This is a preprint, the final version is subject to change, of the American Mineralogist (MSA)
Cite as Authors (Year) Title. American Mineralogist, in press.
DOI: https://doi.org/10.2138/am-2019-7057

Revision 1

High-Pressure Phase and Elasticity of Ammonia Hydrate

XINYANG LI[1], WEIGANG SHI[1], XIAODI LIU[2], ZHU MAO[1*]

[1]Laboratory of Seismology and Physics of Earth's Interior, School of Earth and Planetary Sciences, University of Science and Technology of China, Hefei, China

[2]Key Laboratory of Materials Physics, Institute of Solid State Physics, Chinese Academy of Sciences, Hefei, China

*Corresponding author: zhumao@ustc.edu.cn

Abstract

Phase stability and elasticity of ammonia hydrate have been studied using Raman spectroscopy and Brillion scattering in diamond anvil cells up to 53 GPa and 300 K. Here we have established the high-pressure phase diagram of ammonia hydrate in three different compositions, including ammonia monohydrate (AMH, $NH_3 \cdot H_2O$), dihydrate (ADH, $NH_3 \cdot 2H_2O$), and trihydrate (ATH, $NH_3 \cdot 3H_2O$). In contrast to previous experimental results, our Raman and Brillouin measurements at 300 K have shown that all three ammonia hydrates start to dehydrate at 2.1-2.2 GPa. Dehydration of the ammonia hydrate leads to the formation of single-crystal ice-VII and an increase in the concentration of NH_3 in the residual liquid. The residual liquid finally turns into solid ammonia hemihydrate phase II (AHH-II) at 4-4.6 GPa, leading to a 28% jump in the compressional-wave velocity (V_P). Considering a 10-15 vol.% NH_3 in the mantle of ice giants, AHH should thus be the dominant form of NH_3 coexisting with H_2O-ice in the ice giants. Further Brillouin measurements provide crucial constraints on the V_P of AHH and the single-crystal elasticity of ice-VII at high pressures and 300 K. V_P of AHH increases smoothly with pressure. No anomalous change in V_P of AHH was identified up to 39 GPa, although a solid to solid phase transition was noted to occur at ~18 GPa by Raman measurements. In addition, as the dehydration products of ammonia hydrate, single-crystal elasticity of ice-VII has been determined up to 53 GPa at 300 K. The deviation of C_{12} from C_{44} observed at 11.4 and 14.6 GPa could be caused by the hydrogen bond symmetrisations or the ordering of dipole of single-crystal ice-VII. An abnormal softening in the elastic moduli C_{11}, C_{12}, and the adiabatic moduli K_S together with stiffening in C_{44} was observed between 42 and 53 GPa which should be caused by the transition from ice-VII to its pre-transitional state.

Of particular interest is the dramatic increase in the anisotropy of ice-VII with increasing pressure. Combining the sound velocity of AHH and ice-VII, we have modeled the V_P of ice giants with a volume ratio of 20% AHH and 80% ice-VII in the mantle. The obtained high-pressure phase diagram and elastic properties of ammonia hydrate could contribute to understand the structure of the mantle in the ice giants and satellites.

Keywords: ammonia hydrate, AHH, single-crystal ice-VII, elasticity, phase transition, ice giants

1. Introduction

Hundreds of ice giants with a mean density of ~1 g/cm^3 and up to ten times of Earth's mass have been discovered by recent astronomy observations (e.g. Helled et al., 2011; Rauer et al., 2014; Sotin et al., 2007; Valencia et al., 2007). The mantle of these ice giants, including Neptune and Uranus as well as their large satellites, are expected to be composed by the water-ammonia-methane mixture (e.g. Brown and Calvin, 2000; Fortes, 2012; Nettelmann et al., 2016; Sohl et al.,, 2003). High-pressure studies on the physical properties of the related water mixtures, particular the phase diagram, density, and elasticity, etc., are thus essential in understanding the structure, composition, and evolution of these ice giants and satellites (Choukroun and Grasset, 2010; Dong et al., 2009; Grasset and Pargamin, 2005; Kurnosov et al., 2006).

As one of the potential mantle components in the ice giants, phase stability of ammonia hydrate has been of particular research interest for many years (e.g. Cynn et al., 1989; Fortes et al., 2007; Grasset and Pargamin, 2005; Johnson and Nicol, 1987;

Lunine and Stevenson 1987; Ma et al., 2012a; Sill et al., 1981; Wilson et al., 2012). The high-pressure phase diagram of ammonia hydrate is complicated and strongly depends on the path-compression and the ammonia to water ratio (Fortes et al., 2007; Fortes et al., 2009; Loveday and Nelmes, 1999; Loveday and Nelmes, 2004; Loveday et al., 2009; Ujike and Tominaga, 2002; Wilson et al., 2012). Below 140 K, both ammonia monohydrate ($NH_3{\cdot}H_2O$, AMH) and dihydrate ($NH_3{\cdot}2H_2O$, ADH) crystalize into a single solid phase at high pressures (Fortes et al., 2007; Loveday and Nelmes, 2004; Wilson et al., 2012; Wilson et al., 2015; Fortes et al., 2009; Loveday et al., 2009). Between 140 and 300 K, at least 5 stable phases have been identified for both AMH and ADH at high pressures, respectively (Fortes et al., 2007 Loveday et al., 2009; Fortes et al., 2009; Loveday and Nelmes, 2004; Loveday et al., 2009; Wilson et al., 2015). Since the mantle of ice giants is at high pressures and temperatures, it is more important to explore the high-pressure stability of ammonia hydrate at higher temperatures. An early study which used neutron diffraction showed that liquid AMH would directly transform into the solid AMH-Vb phase at 2.1 GPa and 300 K (Loveday and Nelmes, 2004). In contrast, recent X-ray and neutron diffraction measurements found that elevating pressure leads to the dehydration of liquid AMH to a mixture of solid ammonia hemihydrate phase II ($2NH_3{\cdot}H_2O$, AHH-II) and ice-VII at 3.5 GPa and 300 K(Wilson et al., 2012). It also showed that the solid AMH-Vb phase reported by Loveday and Nelmes,(2004) is AHH-II (Wilson et al., 2012). At 19-26 GPa and 300 K, AHH-II was reported to transform into the disordered molecular alloy (DMA) (Ma et al., 2012a; Wilson et al., 2015). AHH in a sequence of ionic phases was predicted to be stable up to 500 GPa and be a separate phase coexisting with ice in the mantle of ice giants (Robinson et al., 2017).

101 According to the density profile and the nearby planetary nebula of Uranus and
102 Neptune, the ammonia content is predicted to be 10-15 vol.%, indicating a
103 composition of half ADH and half ice in some ice giants (Cavazzoni et al., 1999;
104 Guillot, 2005). However, the phase stability of ADH at high pressures is still under
105 debate (Fortes et al., 2007; Ma et al., 2012a; Wilson et al., 2012). At 300 K, ADH was
106 reported to decompose into ice-VII and the residual liquid at 2.4 GPa by neutron
107 diffraction (Fortes et al., 2007). The residual liquid from the decomposition of ADH
108 further transforms into the AMH phase V (AMH-V) and ice-VII at 3.4 GPa and 300 K
109 (Fortes et al., 2007; Loveday et al., 2009). However, later sound velocity and
110 refractive index measurements have shown that liquid ADH is stable up to 3.2 GPa at
111 300 K, and no dehydration of ADH was observed (Ma et al., 2012b). ADH was
112 reported to follow a similar phase transition path as AMH and would decompose into
113 a mixture of ice-VII and AHH-II at 3.5 GPa and 300 K (Wilson et al., 2015). In this
114 case, AHH should be a separate phase coexisting with ice-VII in the mantle of ice
115 giants and satellites (Wilson et al., 2012; Wilson et al., 2015). More importantly, the
116 sound velocity of AHH is unknown, and the former studied of the sound velocity of
117 ice-VII were mostly focused on the polycrystalline (Ashahara et al.,2010; Kuriakose
118 et al.,2017; Ahart et al.,2011; Zha et al.,1998; Polian et al., 1984). As the synthesis of
119 single-crystal ice-VII was defective, the single-crystal elasticity of ice-VII was only
120 studied below 8 GPa (Shimizu et al., 1995).
121
122 Here, we have studied the high-pressure phase of ammonia hydrate by combining
123 Raman spectroscopy and Brillouin scattering at high pressures and 300 K using
124 diamond anvil cells (DACs). We focused on the phase change of three ammonia
125 hydrates, including AMH, ADH, and ammonia trihydrate (ATH), up to 53 GPa and

300 K. In addition, Brillouin measurements provide crucial constraints on the elasticity of ammonia hydrates and the dehydration product ice VII at high pressures and 300 K. A simple velocity model has been constructed to decipher the structure of ice giants.

2. Experiments

To explore the high-pressure phase of ammonia hydrates, high purity (99.9%) AMH was used as the starting material. Both ADH and ATH were produced by mixing AMH with deionized water in appropriate ratios. Ammonia hydrate was loaded into the diamond anvil cells (DACs) equipped with a pair of Raman ultralow fluorescence diamonds. Rhenium was used as the gasket material, which was pre-indented to a thickness of 30-40 μm. Two ruby spheres were loaded into DACs as the pressure calibrant (Mao et al., 1986). For all three ammonia hydrates investigated here, Raman measurements were performed up to ~30 GPa and 300 K at the High-Pressure Mineral Physics Laboratory in the University of Science and Technology of China (USTC). At each pressure, Raman spectra was collected at five different sample points to observe any potential phase transition and/or dehydration. Meanwhile, high-quality sample photos were taken at each pressure to capture any visual change with increasing pressure.

We have also performed high-pressure Brillouin measurements with a scattering angle of 49.3° using AMH as the starting material up to 53 GPa at 300 K at the High-Pressure Mineral Physics Laboratory in the USTC. The Brillouin signal was excited by a 500-mW laser with a wavelength of 532 nm, while the Brillouin spectra were recorded using a six-pass Sandercock tandem Fabry-Perot interferometer. The

151 acoustic velocities of sample were calculated from the measured Brillouin frequency
152 shift, $\Delta\upsilon_B$, following:

153 $$v = \frac{\Delta\upsilon_B \lambda_0}{2\sin(\theta/2)} \quad (1)$$

154 where v is the acoustic velocity, λ_0 is the laser wavelength of 532 nm, and θ is the
155 external scattering angle measured outside the diamond anvil cell.

156

157 **3. Results**

158 Our high-pressure Raman measurements have revealed that AMH remained in the
159 liquid phase at pressures below 2.2 GPa at 300 K (Figure 1). Above 2.2 GPa, some
160 crystals started to grow from AMH inside the DACs, dividing the sample chamber
161 into two regions (regions A and B) (Figures 1 and 2). Based on the collected Raman
162 spectra, increasing pressure at a rate of 0.1 GPa/10 minutes finally led to the
163 formation of one single-crystal ice-VII which filled the sample chamber excluding
164 AHH (Figures 1 and 3). The precipitation of ice-VII leads to an increase in the
165 concentration of NH_3 in the residual liquid (region A). The residual liquid was noted
166 to completely transform to solid AHH at 4 GPa and 300 K based on the Raman
167 measurements (Figures 1 and 2) (Ma et al., 2012a). Similar to that shown in Ma et al.,
168 (2012a), we also observed the disappearance of the stretching mode ~3342 cm^{-1} at
169 16-18 GPa together with the presence of a new stretching mode at ~3220 cm^{-1}. This
170 change was previously argued to be related to the AHH-II to AHH-DMA phase
171 transition (Ma et al., 2012a; Wilson et al., 2015). No further change in the Raman
172 spectra and modes were observed up to 30 GPa at 300 K. It is interesting to note that
173 both ADH and ATH exhibited the same phase change with pressure as AMH (Figures
174 1 and 4). The precipitation of ice-VII from the liquid ADH and ATH occurred at
175 2.1-2.2 GPa. The residual liquid transformed into the solid AHH at 4-4.6 GPa and

coexisted with one single-crystal ice-VII which filled the left sample volume up to 26 GPa at 300 K (Figures 1 and 4).

We then measured the sound velocity of liquid AMH, solid AHH and ice-VII at high pressures and 300 K using Brillouin scattering (Figures 5, S1, and S2). Here, AHH and ice VII were formed by the dehydration of AMH. We only observed the compressional-wave velocity (V_P) of AHH in our Brillouin measurements (Figure 5). The precipitation of ice-VII from AMH at 2.2 GPa came along with an increase in the concentration of NH_3 in the residual liquid in region A where the composition changed from AMH to AHH. Yet the increase in the concentration of NH_3 did not cause any notable variation in the sound velocity or the velocity gradient of the liquid phase (Figure 5). We further observed a velocity jump in region A from 4.6 km/s at 3.7 GPa to 5.9 km/s at 3.8 GPa which was associated with the formation of solid AHH. To examine the potential anisotropy of the polycrystalline AHH, we rotated the DACs and measured the sound velocity of AHH at a 20 ^{o} step over a range of 180^{o} at each pressure. The variation of V_P over a range of 180^{o} at each pressure was within 10%. Here, we averaged the measured V_P of AHH at each pressure (Figure 5). The upper and lower bounds of V_P are also shown in Figure 5.

Ice-VII precipitated from AMH formed one single-crystal which filled the sample volume excluding AHH. Ice VII is in the cubic structure with space group $Pn\bar{3}m$. Single-crystal Ice-VII is characterized by 3 independent elastic constants, C_{11}, C_{12}, and C_{44} which can be derived by fitting the measured velocity using the Christoffel's equations (Every, 1980) (Figures S1 and S2):

$$\left| C_{ijkl} n_j n_l - \rho v^2 \delta_{ik} \right| = 0 \quad (2)$$

This is a preprint, the final version is subject to change, of the American Mineralogist (MSA)
Cite as Authors (Year) Title. American Mineralogist, in press.
DOI: https://doi.org/10.2138/am-2019-7057

where C_{ijkl} is the full elastic tensor, n_j and n_l are the direction cosines in the photon propagation direction which can be described by the azimuthal angle (θ, χ, ψ) of the sample platelet, ρ is the density, v is the acoustic velocity derived from Brillion frequency shift, and δ_{ik} is the Kronecker delta. Density of ice-VII from previous X-ray diffraction studies was combined with our measured sound velocities to determine the single-crystal elasticity of ice-VII at high pressures (Loubeyre et al., 1999; Sugimura et al., 2008). Our high-quality Brillouin results allow us to well constrain the single-crystal elasticity of ice-VII up to 53 GPa and 300 K (Figure 6 and Table S1). Below 42 GPa, C_{12} nearly equals C_{44} within the experimental uncertainties except at 11.4 and 14.6 GPa. It is worth noting that both C_{11} and C_{12} exhibited an anomalous softening with pressure between 42 and 53 GPa together with an abnormal reduction in C_{44} at this pressure range (Figure 6). Below 42 GPa, the relationship between each C_{ij} and pressure (P) can be described as follows:

$$C_{11} = 27.8(15) + 5.48(15) \times P - 0.173(3) \times P^2$$

$$C_{12} = 14.4(9) + 3.47(3) \times P \quad (3)$$

$$C_{44} = 14.7(14) + 3.35(6) \times P$$

Here, we ignored the data points at 11.4 and 14.6 GPa to derive the pressure dependence of C_{12} and C_{44}. Using the obtained C_{ij}s, we have calculated the adiabatic bulk (K_S) and shear moduli (G) of ice-VII using the Voigt-Reuss-Hill average. Similar to those shown in C_{ij}s, anomalous softening was also observed in K_S between 42 and 53 GPa but is not obvious in G (Figure 6). Below 42 GPa, the pressure-elastic moduli relationship for K_S and G by ignoring the data points at 11.4 and 14.6 GPa is:

$$K_S = 18.3(13) + 4.23(14) \times P - 0.0078(30) \times P^2$$

$$G = 10.3(6) + 2.16(7) \times P - 0.009(1) \times P^2 \quad (4)$$

4. Discussion

4.1. Stability and sound velocity of ammonia hydrate at high pressures

Combining our high-pressure Raman and Brillouin measurements together with the sample photos taken at each pressure, we have found that ammonia hydrate, including AMH, ADH, and ATH, starts to dehydrate at 2.1-2.2 GPa and 300 K. The dehydration of ammonia hydrate investigated here occurs at lower pressure than that reported in previous studies (Loveday and Nelmes, 2004;; Wilson et al., 2012; Wilson et al., 2015). Here we present the first experimental evidence to show how ice-VII gradually precipitates from the ammonia hydrate together with the increase of the NH_3 concentration in the residual liquid (Figure 1) (Loveday and Nelmes, 2004; Wilson et al., 2012; Wilson et al., 2015). In contrast, previous X-ray, neutron diffraction and Raman measurements suggested a direct transformation of AMH (ADH) to ice VII and solid AHH (AMH-V) (Loveday and Nelmes, 2004; Wilson et al., 2012; Wilson et al., 2015). Our experimental results confirm the speculation of Wilson et al., (2012) that ammonia hydrate with an initial H_2O to NH_3 ratio greater than 0.5 will decompose into AHH and ice-VII at high pressures. Together with our Brillouin measurements, we thus conclude that AHH is the stable form of ammonia hydrate above 4-4.6 GPa at 300 K and will coexist with ice-VII at least up to 53 GPa (Figure 4). It should be noted that, although region A experienced a change in the concentration of NH_3 due to the dehydration of AMH, the sound velocity of region A did not exhibit any anomalous change with pressure between 0.3 and 3.6 GPa (Figure 5). In addition, liquid ammonia hydrate in region A has a slightly lower V_P than the pure NH_3, indicating that addition of H_2O can lower V_P of the ammonia hydrate (Figure5) (Li et al., 2009).

Above 4-4.6 GPa, AHH should crystallize in the AHH-II structure which is monoclinic with space group $P2_1/c$ (Wilson et al.,2012; Wilson et al.,2015). Previous experimental study using X-ray diffraction and Raman spectroscopy reported a phase transition from the AHH-II to AHH-DMA phase at 19-26 GPa and 300 K (Ma et al., 2012a; Wilson et al., 2015). Similar to that shown in Ma et al., (2012a), we also observed a change in the Raman stretching modes 3430 cm^{-1}, 3400 cm^{-1}, 3340 cm^{-1} and 3320 cm^{-1} of AHH at ~18 GPa together with the presence of a new mode at ~3220 cm^{-1} for all three ammonia hydrates (Figure 2). The observed variation in the Raman stretching modes could be related to the AHH-II to AHH-DMA phase transition (Figure 2). Our Raman results are consistent with a recent theoretical calculation which found a transition from the AHH-II phase to a energetically competitive quasi-bcc AHH-DMA phase at ~20 GPa, although an X-ray and neutron diffraction study argued that this phase transition should occur at ~26 GPa and 300 K (Robinson et al., 2017; Wilson et al., 2015). It is worth noting that previous experimental studies only observed two broad diffraction peaks for the proposed AHH-DMA phase (Ma et al., 2012a; Wilson et al., 2015). Although the AHH-DMA phase could be stable up to 65 GPa at 300 K, the structure of the AHH-DMA phase cannot be well constrained by limited number of diffraction peaks and thus needs further investigation (Ma et al., 2012a; Robinson et al., 2017; Wilson et al., 2015). In addition, we did not observe any anomalous change in the sound velocity of AHH up to 39 GPa (Figure 5). The polycrystalline AHH in our DACs was not laser annealed and might have developed weak preferred orientations at high pressures. The change in the sound velocity across the phase transition obtained from the polycrystalline AHH sample could be relatively small and cancelled out when we averaged the measured velocity in different

azimuthal angles. The shaded area in Figure 5 provides the estimated errors of our sound velocity measurements for AHH. The change in the sound velocity from AHH and DMA could be within the shaded area and needs to be examined by future studies.

4.2 Sound velocity of ice-VII

As the dehydration product of ammonia hydrate above 2.1 GPa, ice-VII will be an individual phase coexisting with AHH in the mantle of ice giants and satellites (Robinson et al., 2017; Wilson et al., 2012; Wilson et al., 2015). Comparing the Raman modes of ice-VII from the dehydration of AMH to those of ice-VII from pure H_2O has shown that they are indistinguishable from each other within experimental uncertainties (Figure 3). Moreover, the obtained C_{ij}s, K_S, and G of our ice-VII single crystals at 2.8 and 6.7 GPa are in excellent agreement with previous single-crystal measurements for H_2O ice-VII (Figure 6) (Shimizu et al., 1995). This indicates that ice-VII crystallized from the dehydration of AMH has a composition almost the same as that from pure H_2O, or the NH_3 content in our single-crystal ice VII is below the detection limit of the Raman and Brillouin measurements.

Here Brillouin measurements yield crucial constraints on the elasticity and structure of ice-VII at high pressures. Except at 11.4 and 14.6 GPa, C_{12} of ice-VII nearly equals C_{44} up to 42 GPa within experimental uncertainties because of the interaction of atoms by the central forces following the Cauchy relation, consistent with previous single-crystal measurements (Figures 6 and S3) (Shimizu et al.,1995). At 11.4 and 14.6 GPa, C_{12} clearly deviates from C_{44}. A previous single-crystal X-ray diffraction study reported an abnormal change in the *d*-spacing of the superlattice $\frac{1}{2}\frac{1}{2}\frac{1}{2}$ of ice-VII between 10 and 20 GPa, which was interpreted to be caused by the ordering of

dipole following the Ising model (Loubeyre et al., 1999). Recent high-field nuclear magnetic resonance spectroscopy measurements revealed the hydrogen bond symmetrisation of ice-VII at 17 GPa (Meier et al.,2018). We speculate that the deviation of C_{12} from C_{44} observed at 11.4 and 14.6 GPa could be caused by the hydrogen bond symmetrisations or ordering of dipole of single-crystal ice-VII, although Brillouin measurements cannot unravel the variations of hydrous bond with pressures (Loubeyre et al., 1999; Meier et al., 2018).

We also observed an abnormal change in all the C_{ij}s between 42 and 53 GPa which should be caused by the transition from ice-VII to the pre-transitional state ice-VII (Figure 6) (Asahara et al. 2010; Machida et al. 2008; Sugimura et al., 2008). The change from ice-VII to its pre-transitional state was noted to produce an slightly drop in the unit cell volume in the X-ray diffraction experiments (Sugimura et al., 2008). Previous Brillouin measurements using polycrystalline ice-VII reported a sudden drop in the shear-wave velocity, V_S, at 40 GPa in a much narrower pressure range (2 GPa) (Asahara et al., 2010). The sudden drop in V_S was explained to be caused by the change from the ice-VII to its pre-transitional state (Asahara et al., 2010). Here we showed that the variation of ice-VII to its pre-transitional state can barely influence V_S.

The shear modulus, G, is calculated following:

$$\begin{aligned} G_{Voigt} &= (C_{11} - C_{12} + 3C_{44})/5 \\ G_{Reuss} &= 5C_{44}(C_{11} - C_{12})/[3(C_{11} - C_{12}) + 4C_{44}] \\ G &= (G_{Voigt} + G_{Reuss})/2 \end{aligned} \quad (5)$$

Where G_{voigt} and G_{Reuss} are the Voigt and Reuss bound of the bulk (shear) modulus, respectively. As a result, the softening of $(C_{11}$- $C_{12})$ is compensated by the stiffening of C_{44}. No anomalous change in G and V_S is observed between 42 and 53 GPa (Figures 7, S4, and S5). Meanwhile, the anomalous change in V_P is much weaker than the individual C_{ij}s (Figure S5). The reported sudden drop in V_S from polycrystalline

measurements which strongly relied on one data point at 40 GPa with substantial errors is thus highly questionable (Asahara et al., 2010). Furthermore, the change of ice-VII to its pre-transitional state should occur in a wider pressure range than reported in the previous study (Asahara et al., 2010). Single-crystal elasticity of ice-VII has also been determined by a previous study using the measured maximum and minimum V_P of polycrystalline ice-VII (Kuriakose et al., 2017). Such method provided indirect constraints on the single-crystal elasticity of ice-VII at high pressures with much larger errors, which preclude the observation of the abnormal change in C_{ij}s when ice-VII changes into the pre-transitional state (Figure S3) (Kuriakose et al., 2017).

In general, both V_P and V_S of ice-VII calculated from our single-crystal elasticity are in good agreement with polycrystalline measurements below 10 GPa. At higher pressures, our V_P is slightly lower than those from polycrystalline measurements, whereas V_S is greater. Since increasing pressure could change the polycrystalline ice-VII to large anisotropy grains, measuring the acoustic velocity of polycrystalline ice-VII at one direction may introduce large uncertainties at higher pressures (Ahart et al., 2011; Asahara et al., 2010; Polian and Grimsditch, 1984; Zha et al., 1998). V_P and V_S derived from single-crystal elasticity are thus more reliable than those from polycrystalline measurements. Using the obtained single-crystal elasticity, we have calculated the azimuthal compressional wave anisotropy [$A_P=(V_{Pmax}- V_{Pmin})/ V_{Pave}$] and the shear-wave splitting [$A_S^{PO}=(V_{S2}- V_{S1})/ V_{Save}$] of ice-VII at high pressures and 300 K (Figure S6). Both A_P and A_S^{PO} are much greater than those of mantle minerals (e.g. Li et al., 2016; Mao et al., 2015; Mao et al., 2012; Murakami et al., 2007; Sinogeikin et al., 2003). In contrast to silicates, elevating pressure leads to an increase in A_P and

349 A_S^{PO} (Figure S5). A_P of ice-VII increases from 18.1% at 2.8 GPa to 26.9% at 53 GPa,
350 while A_S^{PO} increases from 41% to 65.8%. Due to the dipole ordering between 10 and
351 20 GPa, A_P of ice-VII exhibits a weak softening at this pressure range, while a sudden
352 increase was observed in A_S^{PO} (Loubeyre et al., 1999). The evolution of ice-VII to the
353 pre-transitional state also cause a weak anomalous change in A_P and A_S^{PO} between 42
354 and 53 GPa.
355
356 **5. Implications**
357 The mantle of some icy giants and satellites, such as Uranus, Neptune and Titan, is
358 expected to have an ammonia to water volume ratio of 15:85 (Cavazzoni et al., 1999;
359 Guillot, 2005). After the dehydration of ammonia-water completed above 4 GPa, the
360 mantle of ice giants and satellites is estimated to contain ~80% H_2O-ice and ~20%
361 AHH in volume ratio (Wilson et al., 2012). H_2O-ice is thus the dominant phase in the
362 mantle of ice giants and satellites. Of particular importance is that, although AHH
363 from the dehydration of ammonia-water mixture is normally polycrystalline, ice-VII
364 always forms one nice single-crystal, regardless whether the starting composition is
365 AMH, ADH, or ATH. Ice-VII exhibits anomalous large velocity anisotropies with
366 increasing pressure. Here we evaluate the variations in the sound velocity of the
367 AHH-ice-VII mixture due to the potential lattice preferred orientation of ice-VII in the
368 mantle of ice giants and satellites.
369
370 Considering 20% of AHH and 80% of ice-VII in the mantle of ice giants and
371 satellites, we have further modeled the velocity variation of AHH-ice-VII mixture up
372 to 53 GPa at 300 K with considering the potential anisotropy of ice-VII at high
373 pressures (Cavazzoni et al., 1999; Guillot, 2005). We focus on V_P here because of

374 lacking the experimental constraints on V_S of AHH. Without the density of AHH at
375 high pressures, V_P in the mantle ice giants and satellites was calculated by averaging
376 the velocities of AHH and ice-VII in a 1:4 volume ratio, which represents a first order
377 estimation on the velocity profiles of the ice giants and satellites. Our modeling has
378 shown that the difference in V_P among AHH, ice VII and AHH-ice VII mixture is
379 small below 7 GPa at 300 K (Figure 7). Yet elevating pressure dramatically increases
380 the V_P of AHH above 7 GPa. The difference in V_P between AHH and ice-VII is 1% at
381 10 GPa and increases to 5% at 30 GPa (Figure 7). Addition of AHH thus can
382 effectively increase V_P of the AHH-ice mixture. Moreover, our modeling with 20% of
383 AHH and 80% ice -VII in volume ratio in the mantle of ice giants has shown a
384 non-linear increase of V_P with pressure. The pressure dependence of V_P dramatically
385 decreases when ice VII in the AHH-ice VII mixture evolves to its pre-transitional state.
386 The presence of the pre-transitional state ice-VII also causes a weak softening in the
387 V_P of the AHH-ice-VII mixture between 42 and 53 GPa (Figure 7). Considering the
388 potential lattice preferred orientation of ice VII, we have calculated the maximum and
389 minimum V_P of the AHH-ice-VII mixture in the mantle of ice giants and satellite are
390 shown in Figure 7. The difference in the maximum and minimum V_P of the
391 AHH-ice-VII mixture is 16.8% at 10 GPa and increases to 24.2% at 50 GPa.
392
393 In summary, we have investigated the phase stability and elastic properties of
394 ammonia hydrate using Raman spectroscopy and Brillouin scattering up to 53 GPa
395 and 300 K. Our Raman measurements have shown that any ammonia hydrate with a
396 H_2O to NH_3 ratio greater than 0.5 will start to dehydrate at 2.1-2.2 GPa. The
397 dehydration can cause the formation of ice-VII coexisting with the residual liquid
398 between 2 and 4 GPa. The gradual precipitation of ice-VII also leads to an increase in

399 the concentration of NH_3 in the residual liquid. Yet the variation in the concentration
400 of NH_3 does not cause any notable change in the velocity of the liquid phase. The
401 residual liquid will transform to the solid AHH-II phase at ~4 GPa, leading to a 28%
402 jump in V_P. Further Raman and Brillouin measurements have shown that solid AHH
403 will coexist with ice-VII up to at least 53 GPa at 300 K. Although a change in the
404 OH-stretching modes of AHH was observed at ~18 GPa which may be related to the
405 AHH-II to AHH-DMA phase transition, we did not observe any anomalous variation
406 in V_P of AHH up to 30 GPa at 300 K (Ma et al., 2012a; Wilson et al., 2015).
407 Considering the mantle of a few ice giants with 10-15 vol.% NH_3, AHH should thus
408 be the dominant form of ammonia hydrate coexisting with H_2O-ice in the mantle of
409 these ice giants (Cavazzoni et al., 1999; Guillot, 2005).
410
411 It is interesting to note that ice-VII precipitated from the ammonia-water mixture
412 always forms a nice single-crystal. It allows us to provide the constraints on the
413 single-crystal elasticity of ice-VII up to 53 GPa and 300 K. Although C_{12} of ice-VII
414 nearly equals C_{44} below 42 GPa within experimental uncertainties, the dipole ordering
415 based on the Ising model causes C_{12} to derivate from C_{44} at 11.4 and 14.6 GPa
416 (Loubeyre et al., 1999). Another interesting feature for the elasticity of ice-VII is the
417 unusual softening of C_{11}, C_{12}, K_S and V_P together with the abnormal increase in C_{44}
418 between 42 and 53 GPa. The observed anomalous change in the elasticity between 42
419 and 53 GPa should be caused by the change of ice-VII to its pre-transitional state. Yet
420 no abnormal variation with pressure was observed in both G and V_S because the
421 softening of C_{12} and C_{11} between 42 and 53 GPa is compensated by the stiffening of
422 C_{44}. In contrast to most silicates in the Earth, ice-VII exhibits a dramatic increase in
423 the velocity anisotropy with increasing pressure. We further estimated the variation of

424 V_P for the AHH-ice-VII mixture with a 1:4 volume ratio due to the potential lattice
425 preferred orientations of ice-VII at high pressures. The difference between maximum
426 and minimum V_P of the AHH-ice-VII mixture reaches 24.2% at 53 GPa and 300 K.
427 Future studies are expected to investigate the influence of temperature on the phase
428 diagram and the potential anisotropy of ammonia hydrate and provide new insights on
429 the structure of the ice giants and satellites.
430

431 ## Acknowledgement

432 We acknowledge Fan Wang, Suyu Fu, Menglong Sun and Zengming Zhang for
433 experimental assistance. Z. Mao acknowledges supports from the National Science
434 Foundation of China (41590621 and 41874101), the Strategic Priority Research
435 Program of the Chinese Academy of Sciences (XDB18000000), and the Academic
436 leading talents in the University of Science and Technology of China
437 (KY2080000061). All the experimental data are shown in Table S1 included in the
438 supplementary material., Modeling data are available in the supporting information.
439
440

441 ## Reference

442 Ahart, M., Somayazulu, M., Gramsch, S. A., Boehler, R., Mao, H. K., and Hemley, R.
443 J. (2011). Brillouin scattering of H_2O ice to megabar pressures. The Journal of
444 chemical physics, 134(12), 124517. doi;10.1063/1.3557795
445 Asahara, Y., Hirose, K., Ohishi, Y., Hirao, N., and Murakami, M. (2010).
446 Thermoelastic properties of ice VII and its high-pressure polymorphs: Implications
447 for dynamics of cold slab subduction in the lower mantle. Earth and Planetary Science
448 Letters, 299(3-4), 474-482.
449 Brown, M. E., and Calvin, W. M. (2000). Evidence for crystalline water and ammonia
450 ices on Pluto's satellite Charon. Science, 287(5450), 107-109.
451 Cavazzoni, C., Chiarotti, G. L., Scandolo, S., Tosatti, E., Bernasconi, M., and
452 Parrinello, M. (1999). Superionic and metallic states of water and ammonia at giant
453 planet conditions. Science, 283(5398), 44-46.
454 Choukroun, M., and Grasset, O. (2010). Thermodynamic data and modeling of the
455 water and ammonia-water phase diagrams up to 2.2 GPa for planetary

456 geophysics. The Journal of chemical physics, 133(14), 144502.
457 doi:10.1063/1.3487520
458 Cynn, H. C., Boone, S., Koumvakalis, A., Nicol, M., and Stevenson, D. J. (1989).
459 Phase diagram for ammonia-water mixtures at high pressures: implications for icy
460 satellites. Proceedings of the 19th Lunar and Planetary Sciece Conferece,pp.433-441.
461 Dong, T., Wang, L., Liu, A., Guo, X., Ma, Q., Li, G., and Sun, Q. (2009).
462 Experimental study of separation of ammonia synthesis vent gas by hydrate
463 formation. Petroleum Science, 6(2), 188-193.
464 Fortes, A. D. (2012). Titan's internal structure and the evolutionary
465 consequences. Planetary and Space Science, 60(1),10-17.
466 Fortes, A. D., Wood, I. G., Alfredsson, M., Vočadlo, L., Knight, K. S., Marshall, W.
467 G.et al., (2007). The high-pressure phase diagram of ammonia dihydrate. High
468 Pressure Research, 27(2), 201-212.
469 Fortes, A. D., Wood, I. G., Vočadlo, L., Knight, K. S., Marshall, W. G., Tucker, M. G.,
470 and Fernandez-Alonso, F. (2009). Phase behaviour and thermoelastic properties of
471 perdeuterated ammonia hydrate and ice polymorphs from 0 to 2 GPa. Journal of
472 Applied Crystallography, 42(5), 846-866.
473 Grasset, O., and Pargamin, J. (2005). The ammonia–water system at high pressures:
474 Implications for the methane of Titan. Planetary and Space Science, 53(4), 371-384.
475 Guillot, T. (2005). The interiors of giant planets: Models and outstanding
476 questions. Annual Review Earth Planetary Science, 33, 493-530.
477 Helled, R., Anderson, J. D., Podolak, M., and Schubert, G. (2010). Interior models of
478 Uranus and Neptune. The Astrophysical Journal, 726(1), 15.
479 doi:10.1088/0004-637X/726/1/15
480 Johnson, M. L., and Nicol, M. (1987). The ammonia‐water phase diagram and its
481 implications for icy satellites. Journal of Geophysical Research: Solid Earth, 92(B7),
482 6339-6349. doi:10.1029/JB092iB07p06339
483 Kuriakose, M., Raetz, S., Hu, Q. M., Nikitin, S. M., Chigarev, N., Tournat, V. et al.,
484 (2017). Longitudinal sound velocities, elastic anisotropy, and phase transition of
485 high-pressure cubic H_2O ice to 82 GPa. Physical Review B, 96(13), 134122.
486 doi:10.1103/PhysRevB.96.134122
487 Kurnosov, A., Dubrovinsky, L., Kuznetsov, A., and Dmitriev, V. (2006).
488 High-pressure/high-temperature behavior of the methane-ammonia-water system up
489 to 3 GPa. Zeitschrift für Naturforschung B, 61(12), 1573-1576.
490 Li, X., Mao, Z., Sun, N., Liao, Y., Zhai, S., Wang, Y., Ni, H., Wang, J., Tkachev, S. N.,
491 and Lin J-F. (2016). Elasticity of single‐crystal superhydrous phase B at
492 simultaneous high pressure‐temperature conditions. Geophysical Research
493 Letters, 43(16), 8458-8465.
494 Loubeyre, P., LeToullec, R., Wolanin, E., Hanfland, M., and Hausermann, D. (1999).
495 Modulated phases and proton centring in ice observed by X-ray diffraction up to 170
496 GPa. Nature, 397(6719), 503.
497 Loveday, J. S., and Nelmes, R. J. (1999). Ammonia monohydrate VI: A
498 hydrogen-bonded molecular alloy. Physical review letters, 83(21), 4329-4332.
499 Loveday, J. S., and Nelmes, R. J. (2004). The ammonia hydrates—Model
500 mixed-hydrogen-bonded systems. High Pressure Research, 24(1), 45-55.
501 Loveday, J. S., Nelmes, R. J., Bull, C. L., Maynard-Casely, H. E., and Guthrie, M.
502 (2009). Observation of ammonia dihydrate in the AMH-VI structure at room
503 temperature–possible implications for the outer solar system. High Pressure
504 Research, 29(3), 396-404.
505 Lunine, J. I., and Stevenson, D. J. (1987). Clathrate and ammonia hydrates at high

pressure: Application to the origin of methane on Titan. Icarus, 70(1), 61-77.
Ma, C., Li, F., Zhou, Q., Huang, F., Wang, J., Zhang, M.et al., (2012a). Ammonia molecule rotation of pressure-induced phase transition in ammonia hemihydrates $2NH_3 \cdot H_2O$. RSC Advances, 2(11), 4920-4924.
Ma, C., Wu, X., Huang, F., Zhou, Q., Li, F., and Cui, Q. (2012b). The acoustic velocity, refractive index, and equation of state of liquid ammonia dihydrate under high pressure and high temperature. The Journal of chemical physics, 137(10), 104504. doi:10.1063/1.4751944
Machida, S. I., Hirai, H., Kawamura, T., Yamamoto, Y., and Yagi, T. (2008). Structural changes of filled ice ic structure for hydrogen hydrate under high pressure. The Journal of chemical physics, 129(22), 224505. doi:10.1063/1.3013440
Mao, H. K., Xu, J. A., and Bell, P. M. (1986). Calibration of the ruby pressure gauge to 800 kbar under quasi‐hydrostatic conditions. Journal of Geophysical Research: Solid Earth, 91(B5), 4673-4676.
Mao, Z., Fan, D., Lin, J. F., Yang, J., Tkachev, S. N., Zhuravlev, K., and Prakapenka, V. B. (2015). Elasticity of single-crystal olivine at high pressures and temperatures. Earth and Planetary Science Letters, 426, 204-215.
Mao, Z., Lin, J. F., Jacobsen, S. D., Duffy, T. S., Chang, Y. Y., Smyth, J. R., ... and Prakapenka, V. B. (2012). Sound velocities of hydrous ringwoodite to 16 GPa and 673 K. Earth and Planetary Science Letters, 331, 112-119.
Meier, T., Petitgirard, S., Khandarkhaeva, S., and Dubrovinsky, L. (2018). Observation of nuclear quantum effects and hydrogen bond symmetrisation in high pressure ice. Nature communications, 9(1), 2766.
Murakami, M., Sinogeikin, S. V., Hellwig, H., Bass, J. D., and Li, J. (2007). Sound velocity of MgSiO3 perovskite to Mbar pressure. Earth and Planetary Science Letters, 256(1-2), 47-54.
Nettelmann, N., Wang, K., Fortney, J. J., Hamel, S., Yellamilli, S., Bethkenhagen, M., and Redmer, R. (2016). Uranus evolution models with simple thermal boundary layers. Icarus, 275, 107-116.
Polian, A., and Grimsditch, M. (1984). New high-pressure phase of H_2O: Ice X. Physical review letters, 52(15), 1312. doi:10.1103/PhysRevLett.52.1312
Rauer, H., Catala, C., Aerts, C., Appourchaux, T., Benz, W., Brandeker, A. et al., (2014). The PLATO 2.0 mission. Experimental Astronomy, 38(1-2), 249-330.
Robinson, V. N., Wang, Y., Ma, Y., and Hermann, A. (2017). Stabilization of ammonia-rich hydrate inside icy planets. Proceedings of the National Academy of Sciences, 114(34), 9003-9008.
Shimuzu, H., Ohnishi, M., Sasaki, S., and Ishibashi, Y. (1995). Cauchy Relation in Dense H_2O Ice VII. Physical Research Letters, 74(14). doi:10.1103/PhysRevLett.74.2820
Sill, G., Fink, U., and Ferraro, J. R. (1981). The infrared spectrum of ammonia hydrate: Explanation for a reported ammonia phase. The Journal of Chemical Physics, 74(2), 997-1000.
Sinogeikin, S. V., Bass, J. D., and Katsura, T. (2003). Single-crystal elasticity of ringwoodite to high pressures and high temperatures: implications for 520 km seismic discontinuity. Physics of the Earth and Planetary Interiors, 136(1-2), 41-66.
Sohl, F., Hussmann, H., Schwentker, B., Spohn, T., and Lorenz, R. D. (2003). Interior structure models and tidal Love numbers of Titan. Journal of Geophysical Research: Planets, 108(E12). doi:10.1029/2003JE002044
Sotin, C., Grasset, O., and Mocquet, A. (2007). Mass–radius curve for extrasolar Earth-like planets and ocean planets. Icarus, 191(1), 337-351.

Sugimura, E., Iitaka, T., Hirose, K., Kawamura, K., Sata, N., and Ohishi, Y. (2008). Compression of H_2O ice to 126 GPa and implications for hydrogen-bond symmetrization: Synchrotron x-ray diffraction measurements and density-functional calculations. Physical Review B, 77(21), 214103. doi:10.1103/PhysRevB.77.214103

Ujike, T., and Tominaga, Y. (2002). Raman spectral analysis of liquid ammonia and aqueous solution of ammonia. Journal of Raman Spectroscopy, 33(6), 485-493.

Valencia, D., Sasselov, D. D., and O'Connell, R. J. (2007). Radius and structure models of the first super-Earth planet. The Astrophysical Journal, 656(1), 545.

Wilson, C. W., Bull, C. L., Stinton, G., and Loveday, J. S. (2012). Pressure-induced dehydration and the structure of ammonia hemihydrate-II. The Journal of Chemical Physics, 136(9), 094506. 136. doi:10.1063/1.3686870

Wilson, C. W., Bull, C. L., Stinton, G. W., Amos, D. M., Donnelly, M. E., and Loveday, J. S. (2015). On the stability of the disordered molecular alloy phase of ammonia hemihydrate. The Journal of Chemical Physics, 142(9), 094707. doi:10.1063/1.4913684

Zha, C. S., Duffy, T. S., Downs, R. T., Mao, H. K., and Hemley, R. J. (1998). Brillouin scattering and X-ray diffraction of San Carlos olivine: direct pressure determination to 32 GPa. Earth and Planetary Science Letters, 159(1-2), 25-33.

Figure Caption

Figure 1. Representative Raman spectra and sample photos of ammonia hydrate. (a) AMH; (b) ADH; (c) ATH. Region A is related to the residual liquid after the precipitation of ice-VII from the ammonia hydrate which finally forms to AHH. Region B corresponds to the crystallized ice-VII.

Figure 2. Raman modes of ammonia hydrate at high pressures in region A(see Figure 1). (a) AMH; (b) ADH; (c) ATH. Dashed grey lines show the dehydration of ammonia hydrate, formation of solid AHH, and the potential AHH-II to AHH-DMA phase transition, respectively.

Figure 3. Raman modes of ice-VII. Solid circles: ice-VII formed from the dehydration of AMH (this study); open circles: ice-VII from pure H_2O (this study); blue line: ice-VII in Hsieh and Chien (2015).

590

591 **Figure 4.** Phase diagram of ammonia hydrate. Orange: liquid ammonia hydrate with
592 varying NH_3 to H_2O ratio; red: left liquid ammonia hydrate after the precipitation of
593 ice-VII; blue: AHH; green: ice-VII.

594

595 **Figure 5.** V_P of ammonia hydrate at high pressures and 300 K in region A(see Figure
596 1). Green circles: liquid AMH; blue circles: liquid ammonia hydrate in the ration
597 between AMH and AHH; red region: the polycrystalline of AHH with the upper and
598 lower bounds of velocity; open orange circles: ADH at 296 K (Ma et al., 2012b); open
599 pink circles: ammonia at 297 K (Li et al., 2009).

600

601 **Figure 6.** Elastic moduli of ice-VII at high pressures. (a) Single-crystal elasticity of
602 ice-VII. Green: C_{11}; blue: C_{12}; red: C_{44}; solid circles: this study; open circles: Shimizu
603 et al. (1995); (b) Bulk and shear moduli of ice-VII. Red: bulk modulus, K_S; blue:
604 shear modulus, G; solid lines: our fitting results; dashed lines: anomalous change of
605 the elastic moduli with pressure; open circles: single-crystal elasticity of ice-VII from
606 Shimizu et al. (1995).

607

608 **Figure 7.** Modeled V_P of the AHH-ice-VII mixture at high pressures and 300 K. Red
609 line: ice-VII; blue line: AHH; black line: AHH-ice-VII mixture in a 1:4 in volume
610 ratio; grey line: upper and lower bound of AHH-ice-VII mixture.

This is a preprint, the final version is subject to change, of the American Mineralogist (MSA)
Cite as Authors (Year) Title. American Mineralogist, in press.
DOI: https://doi.org/10.2138/am-2019-7057

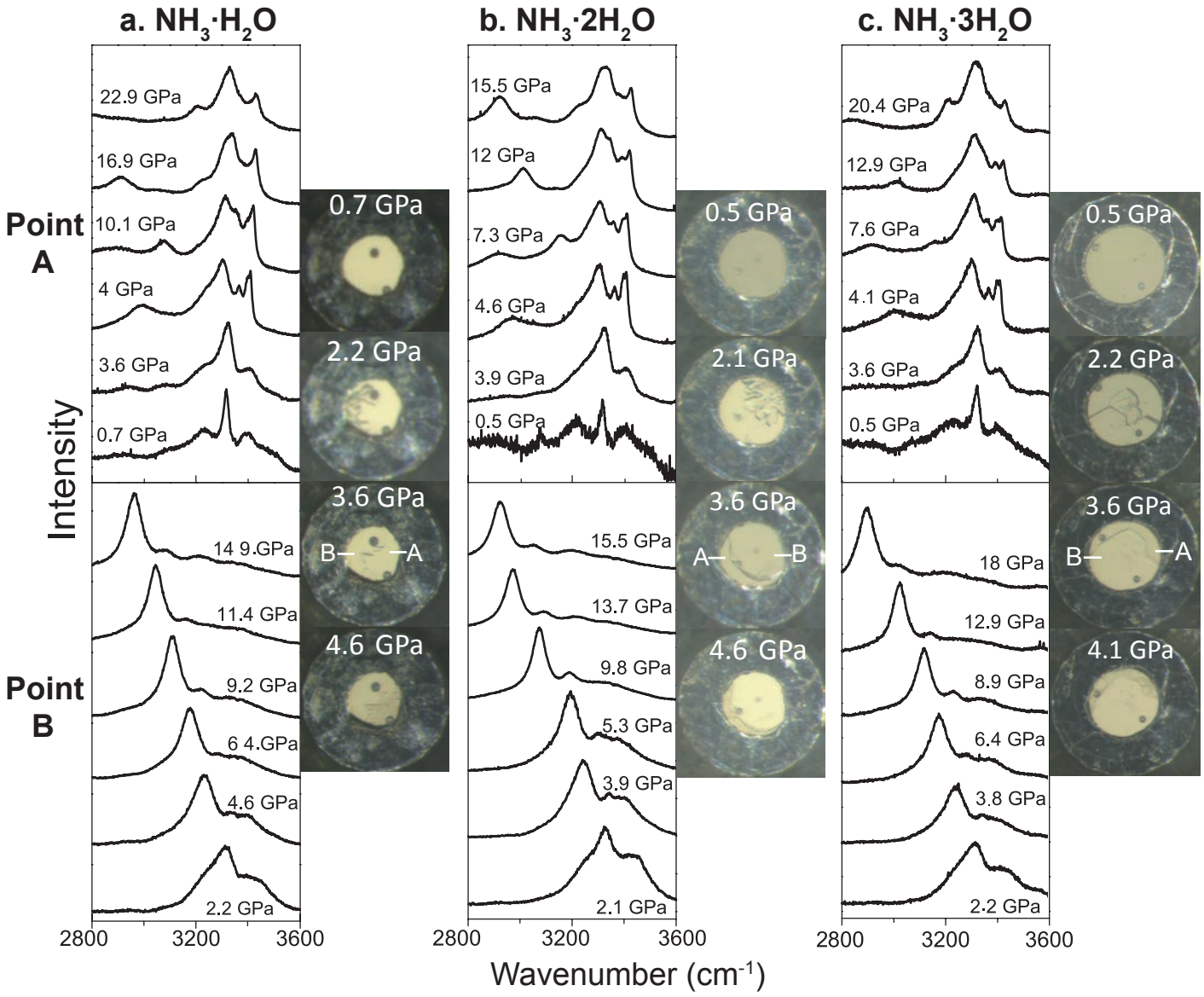

Figure 1

This is a preprint, the final version is subject to change, of the American Mineralogist (MSA)
Cite as Authors (Year) Title. American Mineralogist, in press.
DOI: https://doi.org/10.2138/am-2019-7057

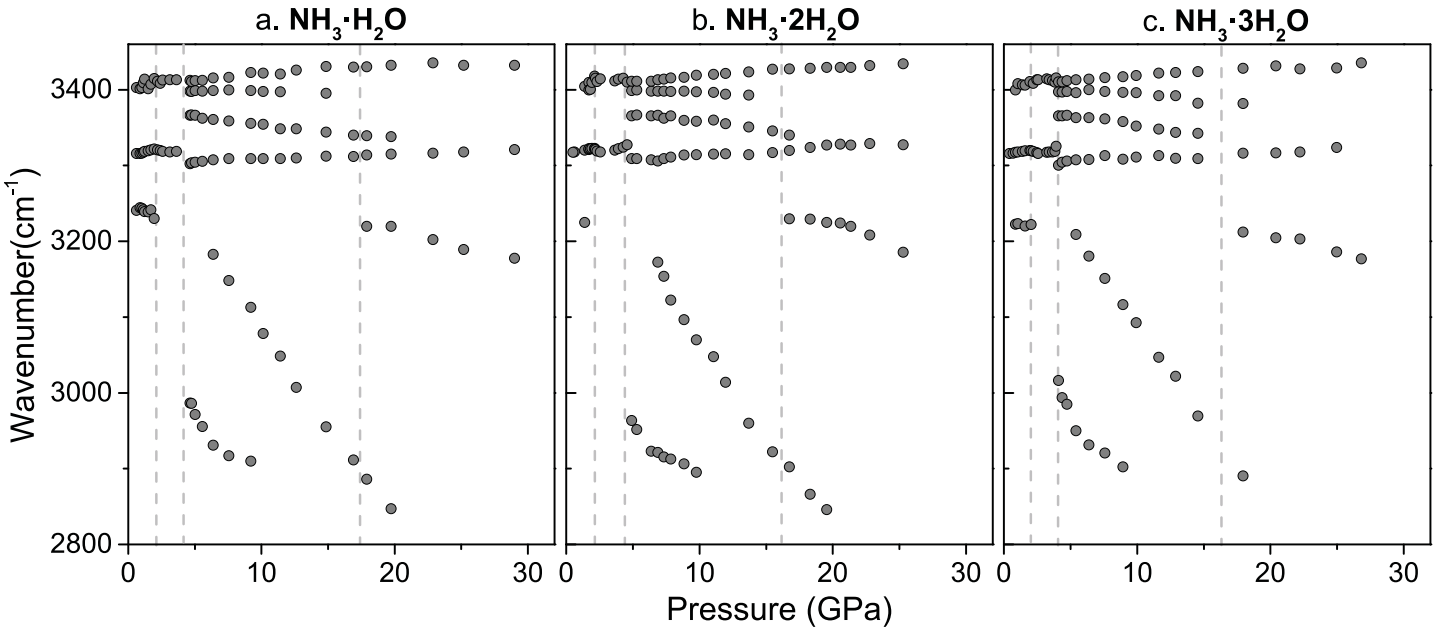

Figure 2

This is a preprint, the final version is subject to change, of the American Mineralogist (MSA)
Cite as Authors (Year) Title. American Mineralogist, in press.
DOI: https://doi.org/10.2138/am-2019-7057

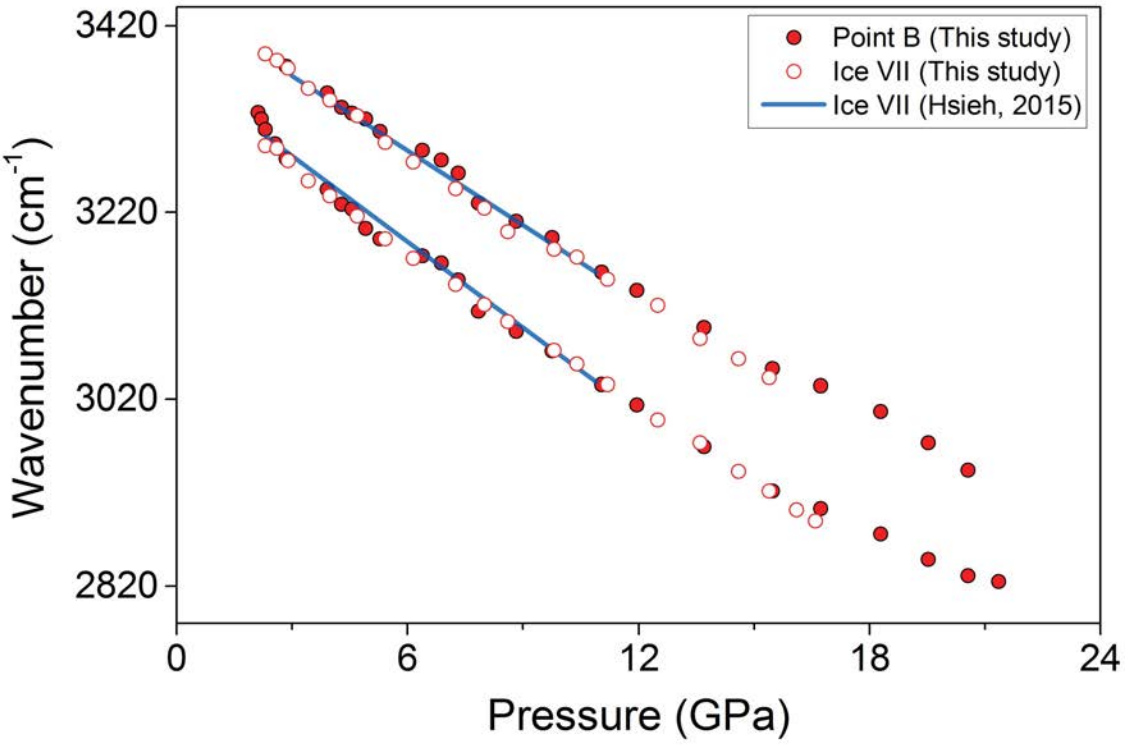

Figure 3

This is a preprint, the final version is subject to change, of the American Mineralogist (MSA)
Cite as Authors (Year) Title. American Mineralogist, in press.
DOI: https://doi.org/10.2138/am-2019-7057

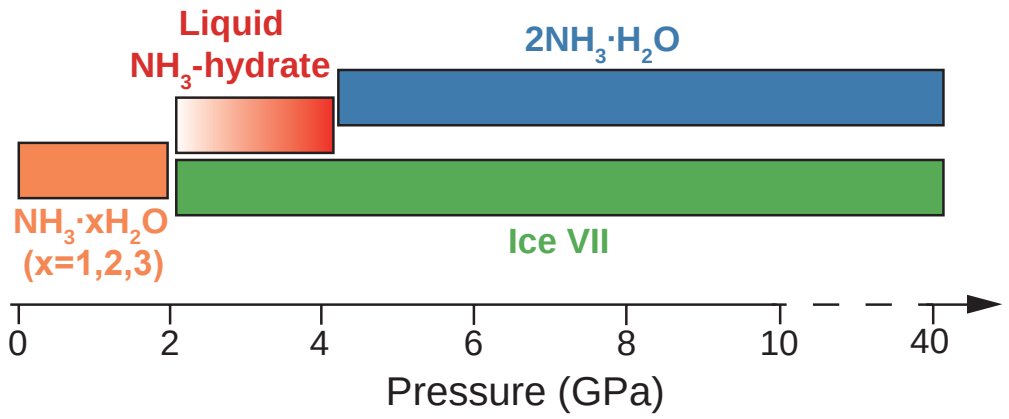

Figure 4

This is a preprint, the final version is subject to change, of the American Mineralogist (MSA)
Cite as Authors (Year) Title. American Mineralogist, in press.
DOI: https://doi.org/10.2138/am-2019-7057

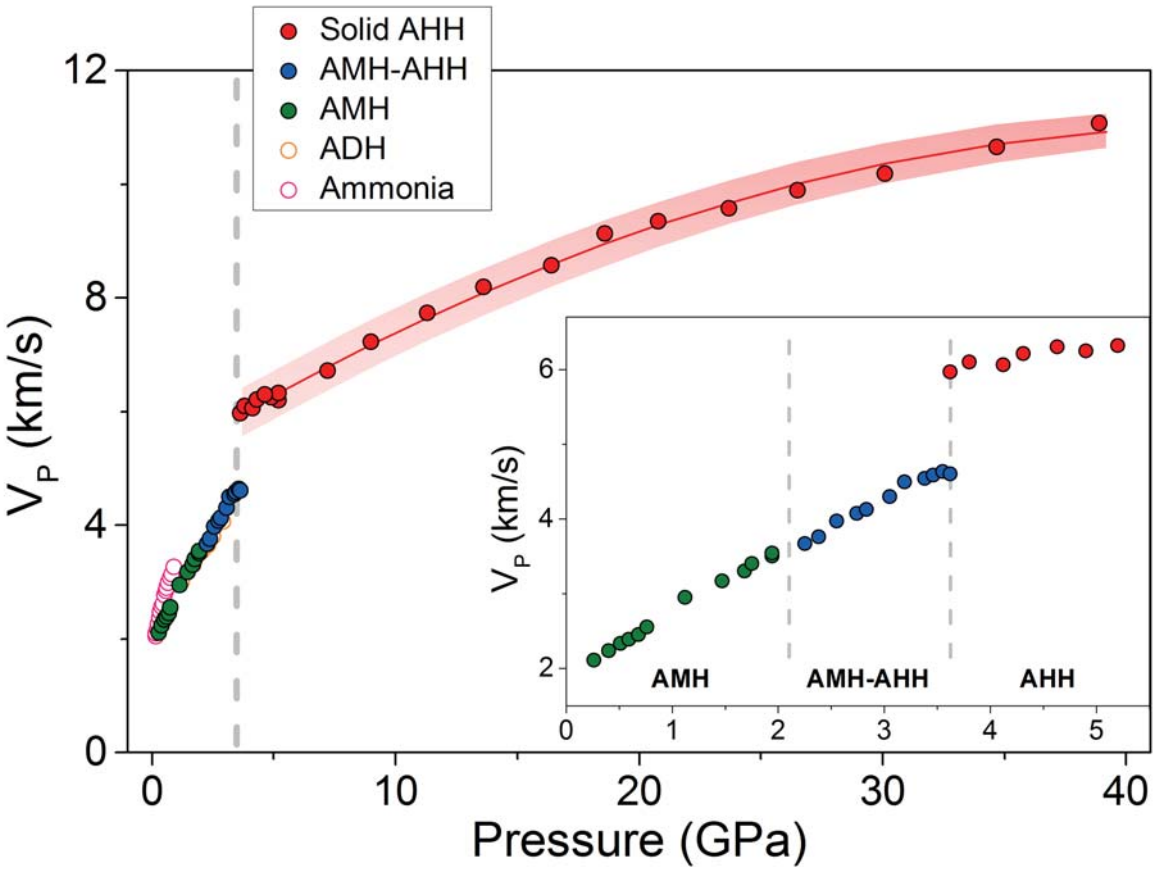

Figure 5

This is a preprint, the final version is subject to change, of the American Mineralogist (MSA)
Cite as Authors (Year) Title. American Mineralogist, in press.
DOI: https://doi.org/10.2138/am-2019-7057

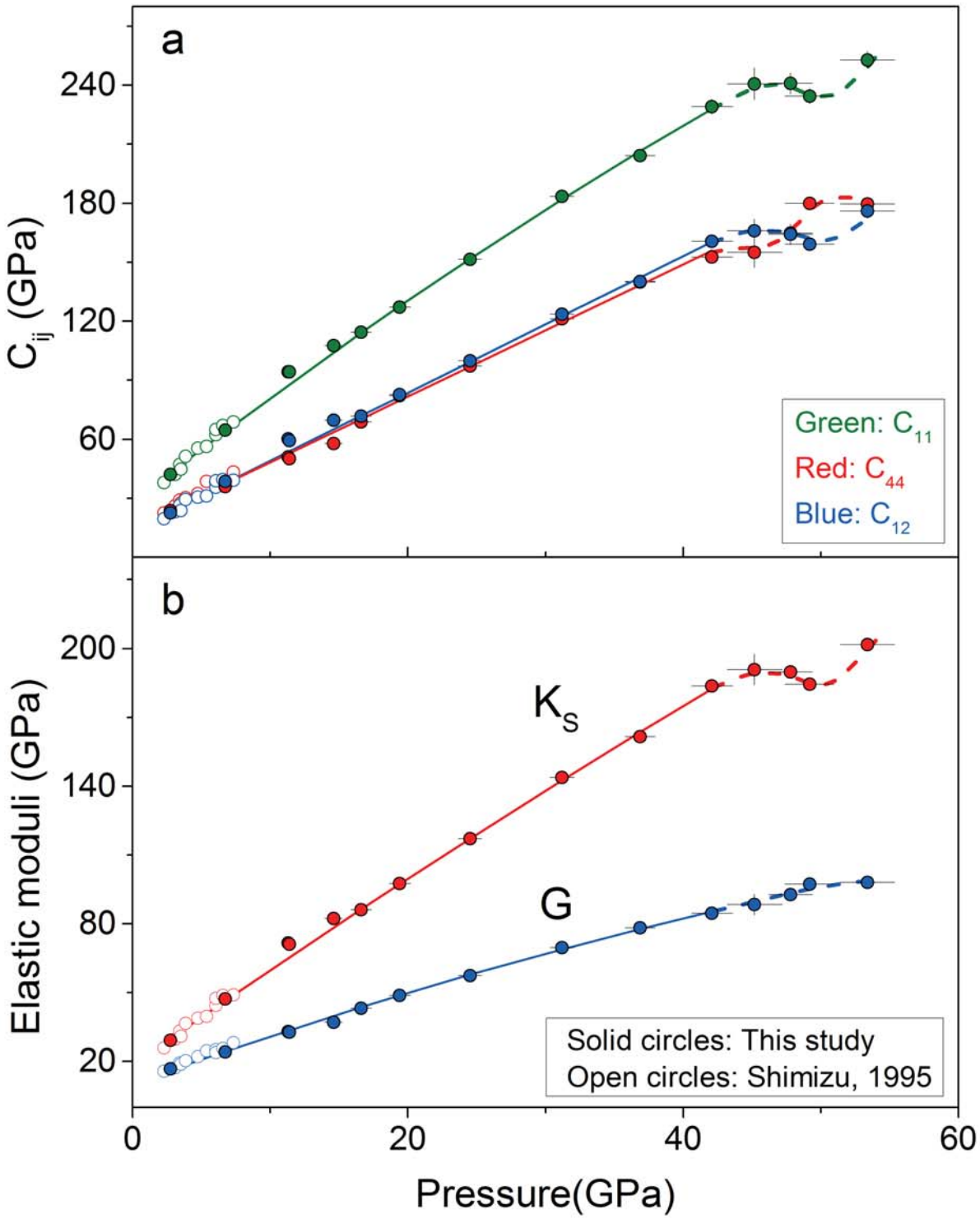

Figure 6

This is a preprint, the final version is subject to change, of the American Mineralogist (MSA)
Cite as Authors (Year) Title. American Mineralogist, in press.
DOI: https://doi.org/10.2138/am-2019-7057